Polymer 71 (2015) 102–112

Contents lists available at ScienceDirect

Polymer

journal homepage: www.elsevier.com/locate/polymer

Rheo-optical characterization of liquid crystalline acetoxypropylcellulose melt undergoing large shear flow and relaxation after flow cessation

Paulo F. Teixeira [a], Susete N. Fernandes [b], João Canejo [b], Maria Helena Godinho [b], José A. Covas [a], Catarina Leal [c, d], Loic Hilliou [a, *]

[a] IPC/I3N – Instituto de Polímeros e Compósitos, Departamento de Engenharia de Polímeros, Universidade do Minho, Guimarães, Portugal
[b] CENIMAT/I3N, Departamento de Ciência dos Materiais, Faculdade Ciências e Tecnologia, Universidade Nova de Lisboa, Caparica, Portugal
[c] ISEL – Instituto Superior de Engenharia de Lisboa, Área Departamental de Física, Lisboa, Portugal
[d] Centro de Investigação em Agronomia, Alimentos, Ambiente e Paisagem – LEAF, Instituto Superior de Agronomia, Universidade de Lisboa, Tapada da Ajuda 1349-017 Lisboa, Portugal

ARTICLE INFO

Article history:
Received 22 April 2015
Received in revised form
26 June 2015
Accepted 30 June 2015
Available online 6 July 2015

Keywords:
Rheo-optics
Cellulose derivative
Liquid-crystal
Extrusion

ABSTRACT

The rheological and structural characteristics of acetoxypropylcellulose (APC) nematic melt are studied at shear rates ranging from 10 s^{-1} to 1000 s^{-1} which are relevant to extrusion based processes. APC shows a monotonic shear thinning behavior over the range of shear rates tested. The negative extrudate-swell shows a minimum when a critical shear rate $\dot{\gamma}_c$ is reached. For shear rates smaller than $\dot{\gamma}_c$, the flow-induced texture consists of two set of bands aligned parallel and normal to the flow direction. At shear rates larger than $\dot{\gamma}_c$, the flow induced texture is reminiscent of a 2 fluids structure. Close to the shearing walls, domains elongated along the flow direction and stacked along the vorticity are imaged with POM, whereas SALS patterns indicate that the bulk of the sheared APC is made of elliptical domains oriented along the vorticity. No full nematic alignment is achieved at the largest shear rate tested. Below $\dot{\gamma}_c$, the stress relaxation is described by a stretched exponential. Above $\dot{\gamma}_c$, the stress relaxation is described by a fast and a slow process. The latter coincides with the growth of normal bands thicknesses, as the APC texture after flow cessation consists of two types of bands with parallel and normal orientations relative to the flow direction. Both bands thicknesses do not depend on the applied shear rate, in contrast to their orientation.

1. Introduction

The most abundant polymer in nature is cellulose, as main constituent of plant cells. It presents a linear structure of β-D-glucopyranose monomers, in which free primary and secondary hydroxyl groups can be fully or partially substituted through esterification or etherification, among other chemical reactions, conferring different chemical configurations to the molecules of the cellulose derivatives [1–3]. The introduction of substituent's groups in the main chain can originate dramatic changes in the chemical and physical properties of cellulose. In particular, cellulose may become soluble in water, or in other solvents, due to the breaking of crystalline chain parts that arises from the inter- and intra-hydrogen bonding among hydroxyl groups. Furthermore, due to the presence of chiral centers in the molecules, the cellulose esters may present a cholesteric liquid crystalline phase, as a lyotropic or as a thermotropic system. When subject to shear, thermotropic cholesteric cellulose esters can present a complex viscoelastic behavior, showing rich anisotropic mechanical properties, as described by Onogi and Asada [4] for liquid crystalline polymers (LCP). These systems may undergo a cholesteric-nematic transition under shear [5] and present generally remarkable optical characteristics [6].

One of the most known cellulose derivatives that can generate liquid crystalline phases is hydroxypropylcellulose (HPC). The thermotropic phase can be observed for a certain molecular weight range in a very narrow temperature window. HPC esterification can induce the temperature scope to increase, starting from below

* Corresponding author.
E-mail address: loic@dep.uminho.pt (L. Hilliou).

http://dx.doi.org/10.1016/j.polymer.2015.06.056
0032-3861/

room temperature up to T = 180 °C, depending on polymer molecular weight and cellulose derivative. The processing of HPC into fibers and films with attractive properties, ranging from energy generation [7] to smart windows [8], essentially relied on wet techniques where HPC as well as HPC esters solutions are first formulated and then processed through knife coating or electrospinning [9]. The smart properties of the resulting cellulose derivatives products stem from changes in the orientational order of the nematic phase, achieved by variation of different external parameters, for example, temperature and UV irradiation [2], as well presence of solvent vapors [7]. Such structural changes give rise to stresses, which result in strains and modifications in film or fiber shape. Evidently, the films or fibers response to external stimuli depends on the liquid crystalline order induced during processing of the material into the final product. As such, the study of the interplay between process parameters and final structural characteristics is central to the design of the smart response to external stimuli.

The effect of shear flow on cellulose derivatives liquid crystalline thermotropic structures was reported a decade ago for acetoxypropylcellulose (APC) [10–12]. Cidade et al. [10], studied APC rheology with a rotational rheometer and explained the complex flow curve by means of a dedicated theory [13]. The flow curve exhibits three regimes. At low shear rates, the nematic polydomain texture is rearranged and partially annealed by the flow: defects break and align along the flow resulting in an almost monodomain texture and a shear thinning behavior is observed. In this flow regime, rheo-optical experiments carried out with a rotational shearing system [11] conveyed slightly different structural information: nematic domains are elongated along the flow direction and dark defects not aligned with the flow appear in polarized optical microscopy (POM). The corresponding small angle light scattering (SALS) patterns show four lobes [11]. At larger shear rates, flow affects the orientational order of APC chains in the monodomain, which is related with a quasi-Newtonian plateau located between 0.2 and 1 s^{-1} [10]. For shear rates in excess of 1 s^{-1}, shear viscosity recaptures a shear thinning behavior, whereas the first normal stress difference, N_1, exhibits an inflexion point in the otherwise monotonic increase with shear rate [10]. Depolarized SALS patterns and POM images captured in this flow regime show a streak aligned along the vorticity direction superimposed on the four lobes. The streak was assigned to striations along the flow and the increased orientation of defects in the vorticity direction was attributed to the opening of the four lobes [11].

After cessation of flow, both studies carried out on thermotropic APC [11,12] reported the formation of a stable band texture that remains during a long period. Band wavelengths with 6–8 μm were observed for a APC sample with molecular mass of 88,000 g/mol [11] and with approximately 2 μm for APC with different molecular masses (52,000 and 62,000 g/mol) [12]. In the latter, this band texture was considered as a "slow band texture", since bands remained observable after 1800 s. The authors also reported a "fast band texture" with wavelength of approximately 10 μm that appears quickly after cessation of shear and then disappears in less than 100 s, depending on temperature [12]. However, these band textures were observed after cessation of shear flows where small shear rate values were imposed (<20 s^{-1}). Furthermore, these structural phenomena have been studied by optical measurements coupled to a rotational shearing system, no *in-situ* measurement of rheological functions having been reported. An important question arises, still without a consistent answer, which deals with the sample behavior at higher shear rates. This shear rate regime is relevant for industrial polymer processes such as extrusion or melt spinning.

The rheological characterization at large shear rates (typically above 100 s^{-1}) of commercial LCPs has been widely documented in the literature. For instance, capillary rheometry showed a shear thinning behavior from 100 to 4096 s^{-1} [14]. Shear thinning was confirmed with slit rheometry, which also showed a non-linear pressure profile along the length of the slit [15] associated with the pressure dependence of viscosity of a commercial nematic LCP. LCPs are known to exhibit very low or negative extrudate swell [16], but its origin is still a matter of debate partly due to the lack of *in-situ* structural characterization, which could confirm either a strain-induced local disorientation of the nematic, or a pressure effect [15]. In this respect, the tumbling (associated with a negative first normal stress difference) or aligning behavior of thermotropic LCP in the high shear regime (regime III) is still an unresolved issue [17,18], and additional experimental data collected with LCP possessing different chain flexibility and chemical structures are still highly needed [19]. On the other hand, the structural characterization of extrudates of commercial LCPs consistently reported a band texture showing up between cross polarizers (see for instance [20] and references therein), but no information is available about band texture formation following the cessation of such fast flows. Indeed, the mechanism of band texture formation after flow cessation is not yet understood, in spite of its high industrial relevance in the fiber industry [21]. Thus, additional experimental data relating the texture time evolution with the material rheology and extrudate characteristics are highly needed to trigger new models.

In this work, we explore the high shear rate regime (regime III) of a thermotropic LCP. We aim at questioning unresolved issues associated with this regime such as: the shear-induced alignment or tumbling of nematic domains, the transition in the sign of the first normal stress difference, the formation and time evolution of band texture after flow cessation and its impact on the ultimate extrudate properties. For this purpose, we characterize, for the first time, the rheo-optical behavior of APC over a wide range of shear rates, using a rheo-optical slit die coupled to a capillary rheometer, thus extending previous efforts [10–12] to larger shear rates. Capillary rheometers equipped with slit dies are the instruments of choice to generate fast flows with polymer melts without possible experimental pitfalls associated with free surface defects (fracture), and to collect rheological data at large shear rates which cannot be achieved with rotational rheometers. Differences in shearing geometries used in previous studies [10–12,14,15,17–19] to generate flow for rheological or optical characterizations are avoided, since the rheological slit die used here allows for the *in-situ* collection of SALS patterns and POM images recorded during steady shear and after flow cessation. In addition, this experimental set-up mimics the extrusion process and allows collecting quenched extrudates at the exit of the die for ex-situ characterization. This unique combination of slit die rheometry with SALS and POM contributes to a better understanding of the rich viscoelastic behavior of APC at flow rates matching the ones found in melt processes such as extrusion. This extensive experimental study documents for the first time the relationships between flow-induced structures, melt rheological characteristics and extrudate properties in a thermotropic LCP.

2. Experimental

2.1. APC synthesis

100 g of (hydroxypropyl)cellulose (HPC) (nominal Mw = 100,000, molar substitution = 3.5 determined by ^{1}H NMR) were added to a three-neck reactor with mechanical stirring and 300 mL of glacial acetic anhydride. Subsequently, 27.5 mL of acetic acid and a catalyst for nucleophilic and esterification reactions were added to the resulting solution. The reactor was heated during eight days and

stirred at 60 °C for periods of 4 h per day. After this time the reaction was quenched with the addition of distilled water and the crude product was washed several times against distilled water until attaining neutral pH. APC was further purified by dissolution in acetone, followed by precipitation in water. The polymer was dried during several days at 60 °C under vacuum until reaching constant weight and a final yield of circa 80% was obtained. The number of acetyl groups per residue, evaluated by ^{1}H NMR, was 2.2 [1,2].

2.2. Rheo-optical experiments

A modular rheo-optical slit die able to measure shear viscosity and normal-stress differences [22], as well as performing in-line SALS and POM [23], was attached on the barrel of a Rosand RH10 capillary rheometer (see Figs. 1 and 2). The rectangular slit (10 × 1 mm) is equipped with a circular optical window (8 mm diameter), two flush mounted pressure transducers to measure the pressure drop and assess the wall shear stress (P_1 and P_2) and a recessed mounted pressure transducer (P_3) to measure normal stress differences through the hole-pressure method [22]. Experiments were conducted at 90 °C and 120 °C. Temperature was controlled by the temperature control system of the rheometer and by separate heating elements of the slit die. In order to calibrate the pressure transducers (Dynisco-type), the die was fed with APC during 1 min and then the material was left to relax until the pressure readings P_1, P_2 and P_3 stabilized. For the measurement of the rheological flow curves, the piston velocity was step varied from 1 mm/min to 500 or 700 mm/min. These correspond to apparent shear rates ranging from 1 s^{-1} to 500 s^{-1}, which were later corrected through the Weissenberg–Rabinowitsch equation to give the true wall shear rate, $\dot{\gamma}$. At low piston velocities, the velocity was increased only after steady state pressure readings were obtained. At larger piston velocities, separate step shear rate experiments were performed, since the whole capillary rheometer reservoir was needed for each. Stress relaxation measurements were only recorded when both steady state pressure reading and a nearly empty reservoir were reached, to minimize effects from material compressibility in the reservoir [24]. With this experimental set-up and protocol, both steady state rheological data and stress relaxation curves upon flow cessation could be recorded, whereas start-up data were discarded due to experimental limitations inherent to the actuation of the piston and melt compressibility [25].

A detailed description of SALS and POM set-ups coupled to the rheometrical slit die and pictured in Figs. 1 and 2 can be found elsewhere [23]. During flow and relaxation, SALS patterns and POM images (1392 pixels × 1040 pixels) were recorded at a rate of 15 fps, with a resolution of 6.45 microns squared by pixel. For both optical configurations, crossed polarizer and analyzer were used with the polarizer aligned along the flow direction. In the case of the relaxation process, films were recorded with a time window of 180 min. For each shear rate, extrudates from the slit die were collected and quenched in iced water for subsequent structural analysis.

2.3. Image analysis

Image analysis using the free software Image J version 1.48p was applied to characterize the texture developing upon relaxation after cessation of shear, as well as the texture of quenched extrudates. Images from the movies recorded during the relaxation process were extracted at 10, 20, 50, 70, 100 and 180 s counted immediately after cessation of shear. Over each image the band texture was characterized considering two directions, parallel and perpendicular with respect to the shear flow direction. The respective angle orientations were also measured. Sufficient measurements were acquired to apply statistical averages and the respective errors were quantified. The extrudates were observed using polarized optical microscopy (POM), between cross polars, and the quenched band structure was also characterized through image analysis.

2.4. Mechanical testing

The mechanical properties of the samples were determined using a tensile testing machine from Rheometric Scientific (Minimat Firmware 3.1). Samples approximately 2 cm long were cut from the extrudates and stretched uniaxially at room temperature in the direction of the previous extrusion, at a speed of 2 mm/min. Tests were generally stopped before rupture occurs and after the maximum stress was overcome.

3. Results and discussion

3.1. Steady shear

APC melt steady shear viscosity computed from the wall shear stress and the true wall shear rate exhibits a monotonic shear-thinning behavior in all the probed shear rate range, as shown in Fig. 3.

The viscosity values decreased with the increase of temperature, as expected, an activation energy $E_a = 2.27 \pm 0.02$ kJ/mol being computed assuming an Arrhenius thermal dependence of the steady shear viscosities plotted in Fig. 3. E_a differs significantly from the barrier energy reported for a APC sample with smaller molecular mass (62000 g/mol) and measured with rotational rheometry at a much smaller shear rate (0.1 s^{-1}) [12]. For comparison with previous reports, the steady viscosity was measured at 120 °C at lower shear rates using a stress controlled rotational rheometer (ARG2, TA Instruments) equipped with 25 mm parallel plates. A 1 mm thick sample was used. The corresponding viscosity data displayed in Fig. 3 match the viscosity data reported elsewhere for shear rates of the order of 0.1 s^{-1} [12]. However, the video monitoring of the steady shear test shows that edge fracture occurs for shear rates beyond 0.2 s^{-1}. As such, the plateauing in shear viscosity reported by Cidade et al. [10] cannot be reproduced and the range of shear rates probed with rotational rheometry does not overlay the range probed with slit rheometry. Nevertheless, the steady shear viscosity measured at 10 s^{-1} with slit rheometry matches nicely the steady shear viscosity measured with cone and plate for a very similar sample (Mw = 94,000 g/mol) [10]. The viscosity shows a monotonic shear-thinning behavior from 10 to 1000 s^{-1} which does not depend on temperature: experimental data were fitted to a power law with shear thinning exponents $n = 0.57 \pm 0.02$ at 90 °C and $n = 0.57 \pm 0.01$ at 120 °C. These exponents slightly differ from the exponent 0.5 predicted and measured for polymers following a Rouse dynamics [26] and from the 0.8 exponent widely reported for entangled polymer melts [27]. Such discrepancy comes as no surprise since the nematic order in APC is predicted to couple with the shear rate in a rather complex way where tumbling or alignment of domains or APC chains can take place [17–19]. However, we can compare the exponents reported in Fig. 3 with the crude scaling behavior predicted for a flow-aligning nematic with homeotropic orientation at the shearing surfaces [19]. At large enough shear rates where the homeotropic orientation is confined in a layer close to the surface due to the nematic alignment along the flow, the viscous contribution of the former is still larger than the latter and a shear thinning behavior with exponent 0.5 is predicted. Within this picture, data in Fig. 3 suggest that no full chain alignment resulting in a large nematic monodomain with director aligned along the

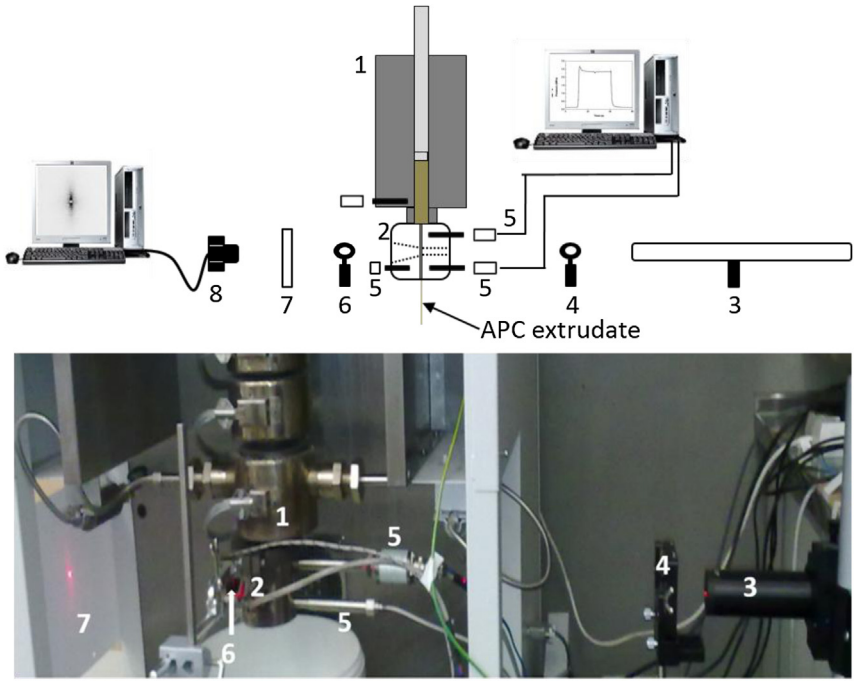

Fig. 1. Rheo-optical set-up for SALS: 1 – Barrel of the capillary rheometer; 2 – Rheo-optical slit die; 3 – He–Ne laser; 4 – Polarizer; 5 – Flush mounted pressure transducers; 6 – Analyzer; 7 – Screen; 8 – CCD camera.

flow is achieved even at 1000 s^{-1}, since no viscosity plateau is observed.

This result is confirmed by the representative POM image captured at 90 °C, at a shear rate of 697 s^{-1} (see Fig. 4b). It reveals a texture with dark and light domains elongated in the flow direction and stacked along the vorticity. This is consistent with striations along the flow imaged in a previous study for shear rates up to 5 s^{-1} [11]. No dark defects aligned along the vorticity are imaged. The blurring effect related to fast motion of objects at such large shear rates together with the slow exposure time for capturing the POM snapshot could hamper proper imaging of the dark defects. The top inset in Fig. 4b shows the two dimensional fast Fourier transform (FFT) computed from the POM displayed in Fig. 4b. The vertical and horizontal thick lines correspond to the FFT windowing, and thus

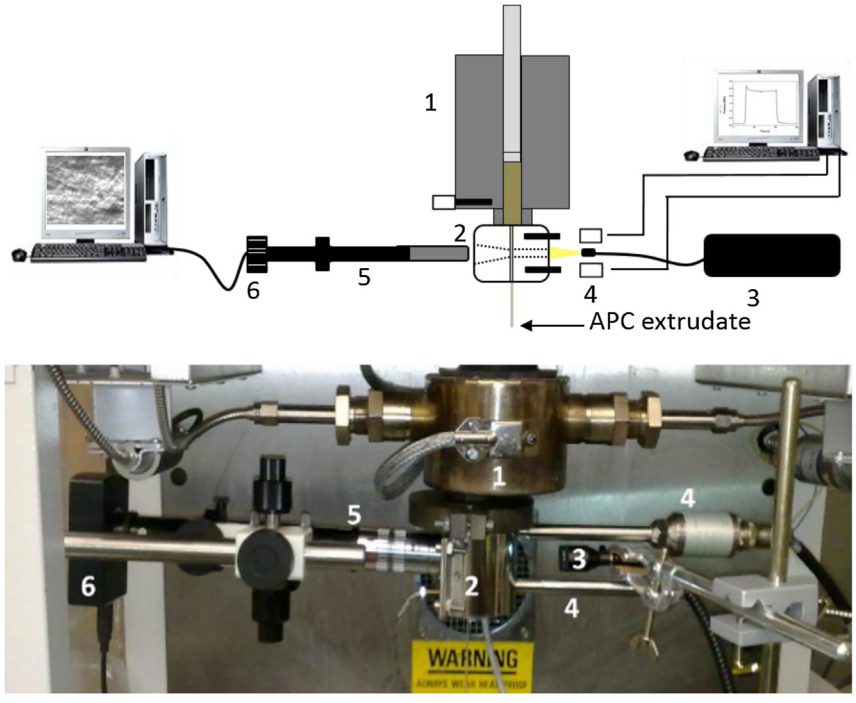

Fig. 2. Rheo-optical set-up for POM: 1 – Barrel of the capillary rheometer; 2 – Rheo-optical slit die; 3 – Source of polarized light; 4 – Flush mounted pressure transducers; 5 – Microscope tube lens and objective connected to a CCD camera (6).

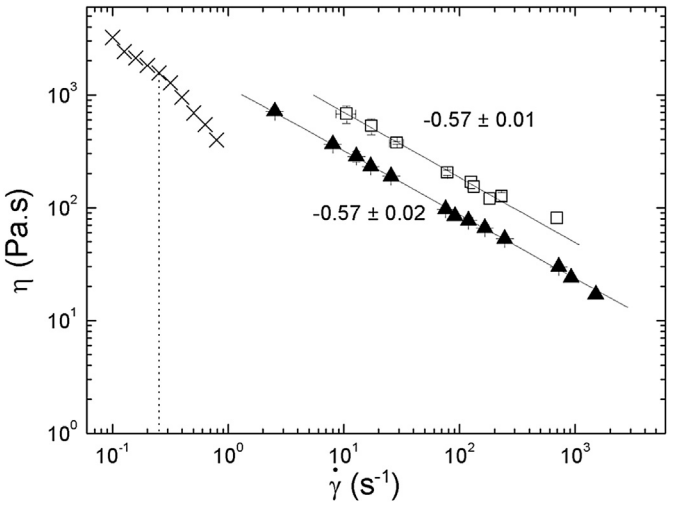

Fig. 3. Shear rate dependence of the steady shear viscosity of APC at 90 °C (open symbols) and at 120 °C (solid symbols); lines are power law fits to the data. Crosses are steady shear viscosity data measured at 120 °C with a rotational rheometer; the vertical dot line indicates edge fracture of the sample.

show up in all FFT displayed in Fig. 4. As expected, a nearly horizontal fine streak and a central elliptical pattern with orientation nearly along the vorticity relate to the striations pictured in the POM image. Similar POM results were found at 120 °C, for the highest shear rates reached in this study (see Fig. 4d). The SALS patterns recorded at 90 °C for the higher shear rate (bottom inset Fig. 4b) are formed by two lobes. Qualitatively similar patterns are also recorded for the fastest flow at 120 °C (bottom inset in Fig. 4d). These SALS patterns contrast with earlier reports [11], where four lobes and a streak were reported, but we note that here the applied shear rates are a hundred times larger. Two lobe patterns were found in polymer solutions undergoing shear-induced demixing [28] and were assigned to the formation of polymer rich ellipsoidal domains in a preferred direction. The orientation of the two lobes displayed here is along the flow direction. By analogy with sheared polymer solutions, this suggests that the ellipsoidal long axis of a scattering domain is normal to the flow direction and that the domains are predominantly formed in that direction. As such, SALS patterns recorded at larger shear rates are consistent with the defects imaged by Riti et al. [11] using POM at shear rates up to 5 s^{-1} and aligned normal to the flow.

The structures imaged by POM in Fig. 4b and d are not consistent with the SALS patterns displayed in the corresponding bottom insets, as suggested from the computed FFT of the POM pictures (see corresponding top insets in POM pictures). Several experimental considerations could explain this mismatch. First, POM images the structures developing close to the optical window of the slit, where the shear gradient is largest, in contrast to SALS, which probes the whole channel depth (1 mm). Second, SALS probes smaller length scales than POM and the length scale of the stacking might fall outside the range of angles probed in SALS (too large structure). Indeed, POM suggests that stacking periodicity as large as 50 microns is at play, which corresponds to angles buried in the beam stop (see white central dots in SALS patterns). Nevertheless, the main output of the rheo-optical characterization given in Figs. 3 and 4 for larger shear rates is that no Newtonian plateau is observed and, consequently, no fully aligned nematic large monodomain along the flow is pictured. This is in contrast with theoretical considerations [13].

At lower shear rates, both POM images and SALS patterns are different. At 90 °C (Fig. 4a) alternating dark and bright structures elongated along the vorticity direction and stacked along the flow are pictured by POM, along with vertical bright and dark structures showing a coarser stacking along the vorticity direction. Qualitatively similar images are captured at 120 °C (Fig. 4c), but with more detail for the vertical structures, which show thinner spacing than the horizontal ones. The quantitative differences in spacing are more evident when comparing the corresponding FFT (see top insets in Fig. 4a and c). The two FFT suggest that the corresponding SALS are consistent with the structures imaged in POM, as all show

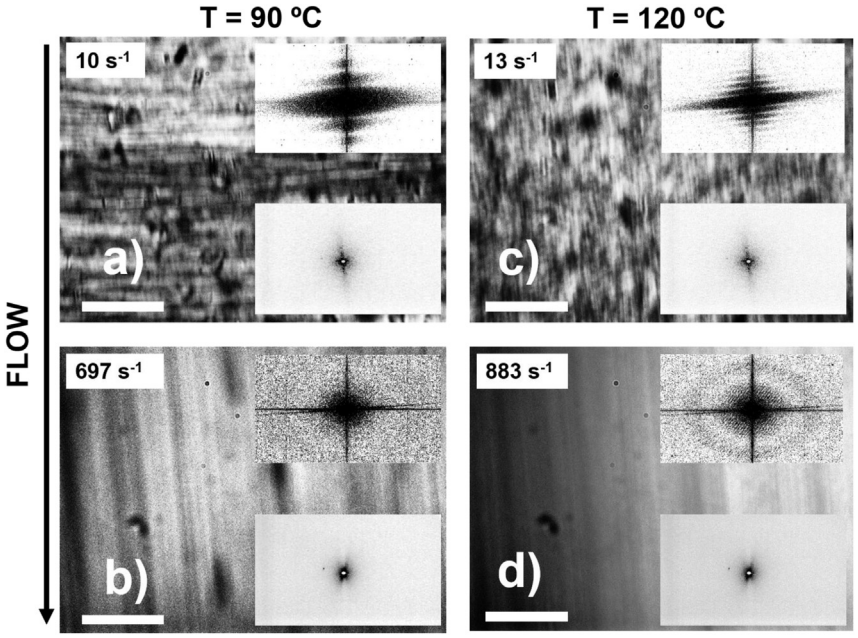

Fig. 4. Representative POM images and SALS patterns (bottom insets) captured during the measurement of the flow curves at 90 °C (a) and (b) and at 120 °C (c) and (d) at the shear rates indicated in the POM images. The top insets are the FFT of the respective POM image. The flow develops in the vertical direction, from top to bottom. The white scale bars correspond to 50 micron.

a streak oriented along the flow, being more intense at 90 °C. However, SALS patterns do not show the superimposed horizontal bright and dark bands computed in the FFT of the POM images. Again, differences in length scales probed by the two techniques explain the discrepancies. Similarities with structures reported by Riti et al. [11] for a nearly identical shear rate range include the defects in the direction normal to the flow, with spacing of the order of 10 microns and the streak in SALS. Nevertheless, the latter was oriented along the vorticity and was assigned to the striations along the flow, which is in contrast to the SALS patterns displayed in the top row of Fig. 4.

Overall, the results in Fig. 4 suggest that the sheared APC presents a complex and hierarchical structure comprising micron and nanosized defects, which are rearranged (oriented, broken and dispersed) into a finer structure at larger shear rate generating a shear thinning behavior. This justifies why scattering at smaller angles is absent at larger shear rates, since these smaller defects scatter light at larger scattering angles. In addition, the structural rearrangement at larger shear rates is accompanied by a reorientation of the coarser structure along the flow, as evidenced by the stacking of defects in POM images, whereas the smallest shear-induced structures are oriented along the vorticity, as suggested by the orientation of the two lobes in SALS patterns. Bands oriented along the vorticity coexisting with bands aligned along the flow are new features. These were not reported for thermotropic and lyotropic liquid crystalline polymers studied at much slower shear rates by shearing much thinner APC samples [11]. An alternative interpretation to the lack of Newtonian behavior and to the complex structural organization at large shear rates may be offered based on the two fluids hypothesis [15,16]. The development of two layers of oriented fluids flowing at different rates in the slit was proposed to explain the negative extrudate-swell observed in liquid crystalline polymers [16] and the skin-core morphology of the corresponding extrudates [1,20,22–25,29,30]. Following this scenario, POM images should be characteristic of the fluid layer developing close to the slit wall, whereas the SALS patterns mostly probe the structure of the central fluid. Within the two fluids hypothesis, the two techniques should provide distinct morphological information, as suggested in Fig. 4. Therefore, it seems relevant to characterize the APC extrudates.

3.2. Characterization of the extrudates

Extrudates quenched after exiting the slit die exhibited a frozen band texture in the direction perpendicular to the previous flow direction. The bulk textures of two extrudates collected at 90 °C for two different shear rates are illustrated in Fig. 5. These textures show similarities with those of liquid crystalline fibers spun from cellulose derivatives [29,30]. No bands aligned along the direction of extrusion could be imaged with the magnification used and within the shear rate range studied. Instead, bands are aligned along the extrudate width (and are thus perpendicular to the flow direction) and stacked along the extrusion direction (machine direction). The band width is of the order of 2–4 μm, regardless of the applied shear rate. These widths are in harmony with those measured at early times after flow cessation in the slit die (see Fig. 11 below), suggesting that the bulk texture of the extrudates corresponds to the relaxing texture quenched within few seconds. Unfortunately, no core-skin morphology could be imaged either with POM or scanning electron microscopy carried out on transversal and longitudinal sections cut from the extrudates.

Fig. 6 presents the shear rate dependence of the extrudate dimensions scaled to the slit width (w_0) and thickness (t_0), at 120 °C and 90 °C. A negative extrudate-swell is observed, i.e., the width and thickness of the extrudates are smaller than the equivalent dimensions of the die, except for the width of extrudates produced at 90 °C with the largest shear rates (see below). The negative extrudate-swell was anticipated from earlier reports for LCPs [16], and the flow-induced structures displayed in Fig. 4. The data in Fig. 6 consistently show an increase of t/t_0 with shear rate at the lower shear rate range. Then, at a critical shear rate ($\dot{\gamma}_c$) identified by vertical dotted lines in Fig. 6, the thickness of the extrudates goes through a minimum. At 120 °C, $\dot{\gamma}_c$ is roughly 50 s^{-1}, whereas it is of the order of 120 s^{-1} at 90 °C. The critical shear rate does not relate to any specific event in the monotonic power law decay of shear viscosity with increasing shear rate (Fig. 3), but separates two flow regimes (slow and fast) where SALS data evidence changes on the flow-induced structure of the APC melt. The negative thickness swell is more important at 90 °C than at 120 °C, which is to be expected, as the nematic elastic forces driving the negative swelling effect should be larger at lower temperatures. The width-swell behaves differently: at 90 °C, a transition from negative to positive values occurs at $\dot{\gamma}_c$. At 120 °C, width-swell remains negative, albeit increasing with shear rate. Apparently, the transition from negative to positive swell has never been reported for thermotropic nematic polymers. It could be related to the change in the sign of the first normal stress differences widely reported for lyotropic liquid crystalline polymers [19]. Unfortunately, elastic effects in the slit die are too small and no normal stress differences (first and second) could be measured with the hole-pressure method used in a separate study on polyethylene and polystyrene [22].

Representative results from tensile testing of the extrudates processed at 120 °C are displayed in Fig. 7. At the lowest strain range, the stress shows two linear regimes (see the left inset in Fig. 7 for a zoomed view): first, the stress grows rapidly and then a more gradual increase sets in. The latter was used to compute the Young's modulus, the values being plotted as a function of shear rate in the right inset in Fig. 7 for the two sets of extrudates produced at 120 °C and 90 °C. The moduli seem to be independent of shear rate, thus suggesting that the flow-induced structural changes that gave rise to changes in extrudate-swell are not mirrored in the ultimate mechanical properties. On the other hand, this result is consistent with the constant band width observed in the extrudates which, as seen in Fig. 5, exhibit nearly similar bulk structure. Also, processing temperature does not significantly impact on the Young's moduli. At larger strains, the tensile stress shows a maximum, followed by a strain softening behavior. The maximum stresses are of the order of 0.2 ± 0.05 MPa (at 0.45 ± 5% strain) and are virtually independent of shear rate and processing temperature.

POM imaging performed after the mechanical testing of the extrudates reveals bands structures essentially similar to those pictured in Fig. 5. All band widths fall in the range 2–4 μm for the extrudates processed at 90 °C. Note here that stretched extrudates present little necking and nearly no strain recovery. This behavior can be attributed to the material liquid crystalline structure [32].

3.3. Stress and bands relaxation after flow cessation

To characterize the relaxation process of APC after cessation of shear flow, pressure drop and in-situ POM and SALS were used. The results obtained for the fade out of the normalized pressure drop (with respect to the steady state value under steady flow) are represented in Fig. 8. For the sake of clarity, only post-flow values are presented. As the temperature increases, the overall behavior of the relaxation curves is shifted to shorter times, but the shape of the curves is qualitatively maintained. Relaxation is sensitive to the intensity of the previous shear flow and has different characteristics below and above a critical shear rate ($\dot{\gamma}_c$). Indeed, at $\dot{\gamma}_c$ stress relaxation changes from a single to a dual process. $\dot{\gamma}_c$ is

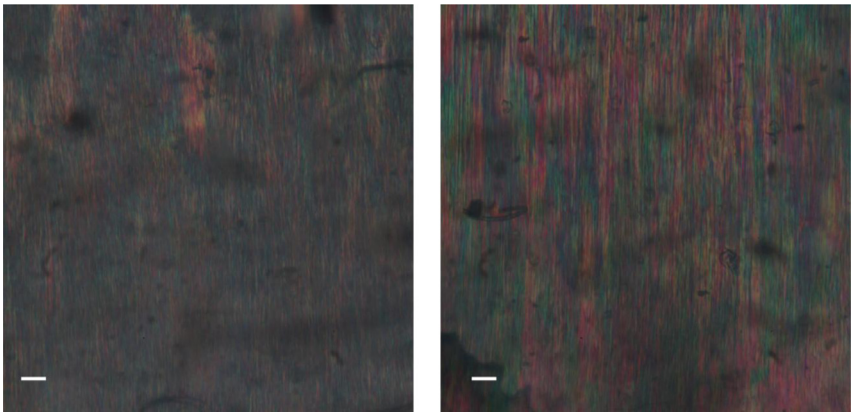

Fig. 5. POM pictures of the quenched bulk textures of two extrudates collected at 90 °C for shear rates of 76 s^{-1} (left) and 883 s^{-1} (right). The white scale bars correspond to 50 micron. The machine direction is horizontal: the extrudate width is along the vertical direction, the extrudate length is in the horizontal direction and the extrudate thickness is normal to the image plane.

temperature dependent, taking the values of 123 s^{-1} and 53 s^{-1} at 90 °C and 120 °C, respectively, although no corresponding event is observed in the flow curve (Fig. 3). These values are in excellent agreement with the critical shear rates obtained from the shear rate dependence of extrudate-swell (see Fig. 6). This clearly indicates that shear stress relaxation and normal stress relaxation (which is associated with extrudate-swell) follow a similar shear rate dependence.

Above $\dot{\gamma}_c$, data in Fig. 8 suggests that stress relaxation splits into a faster process at shorter times, followed by a slower process. Relaxation times were extracted from the stress relaxation data using a stretched exponential function (Equation (1)) for shear rates below $\dot{\gamma}_c$ and two exponentials above $\dot{\gamma}_c$ (Equation (2)),

$$A(t) \approx Ae^{-\left(\frac{t}{\tau}\right)^{\beta}} \tag{1}$$

$$A(t) \approx A_1 e^{-\left(\frac{t}{\tau_1}\right)} + A_2 e^{-\left(\frac{t}{\tau_2}\right)} \tag{2}$$

as no satisfactory fit could be obtained with the stretched exponential.

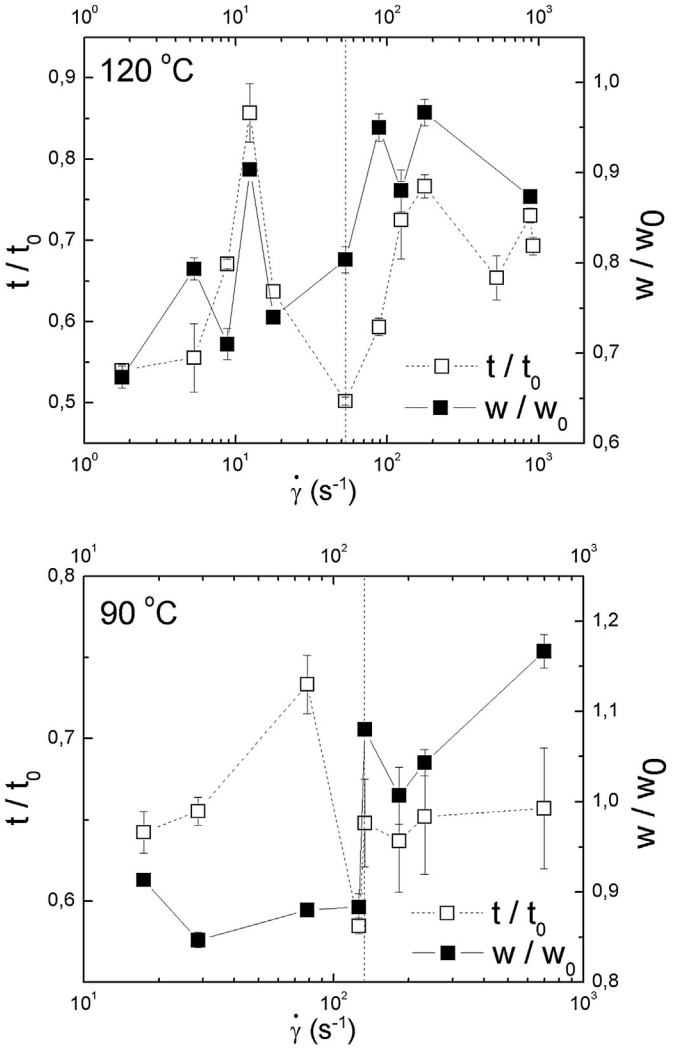

Fig. 6. Extrudate-swell of APC after quenching from 120 °C (top) and 90 °C (bottom): widths w and thicknesses t were scaled to the slit width (w_0) and thickness (t_0), respectively.

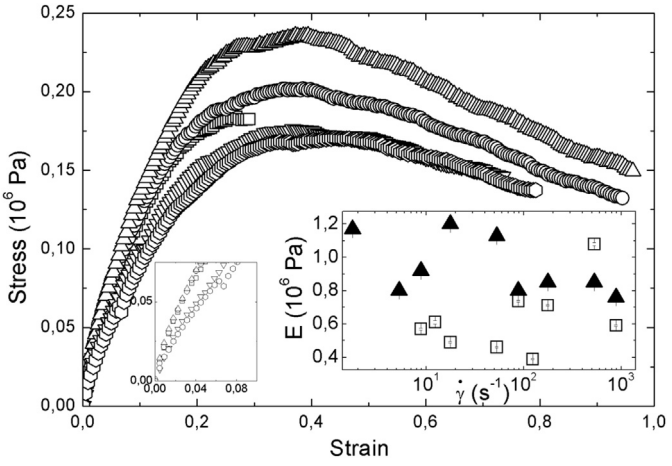

Fig. 7. Stress–strain curves for APC extrudates processed at 120 °C under the following shear rates: 9 s^{-1} (squares), 18 s^{-1} (circles), 53 s^{-1} (triangles), 88 s^{-1} (reversed triangles) and 531 s^{-1} (diamonds). The left inset zooms the stress–strain curves at the lowest strain range. The right inset depicts the variation of the Young's modulus of extrudates produced at 120 °C (solid triangles) and 90 °C (open squares) with shear rate.

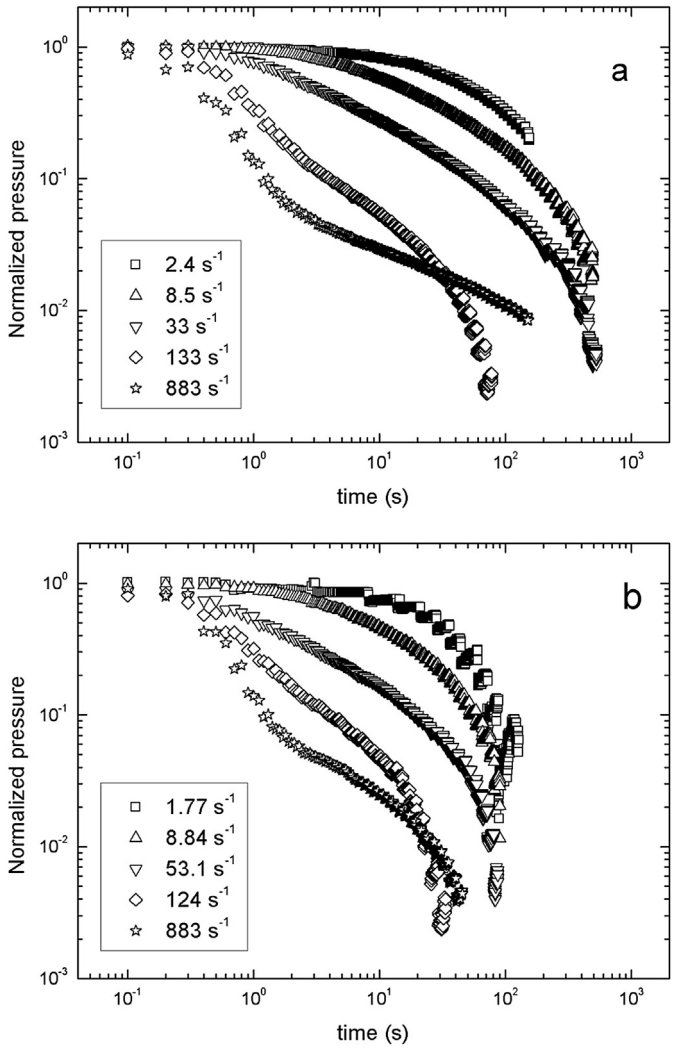

Fig. 8. Relaxation of the normalized pressure drop upon cessation of flow at the indicated shear rates, for APC at 90 °C (a) and 120 °C (b).

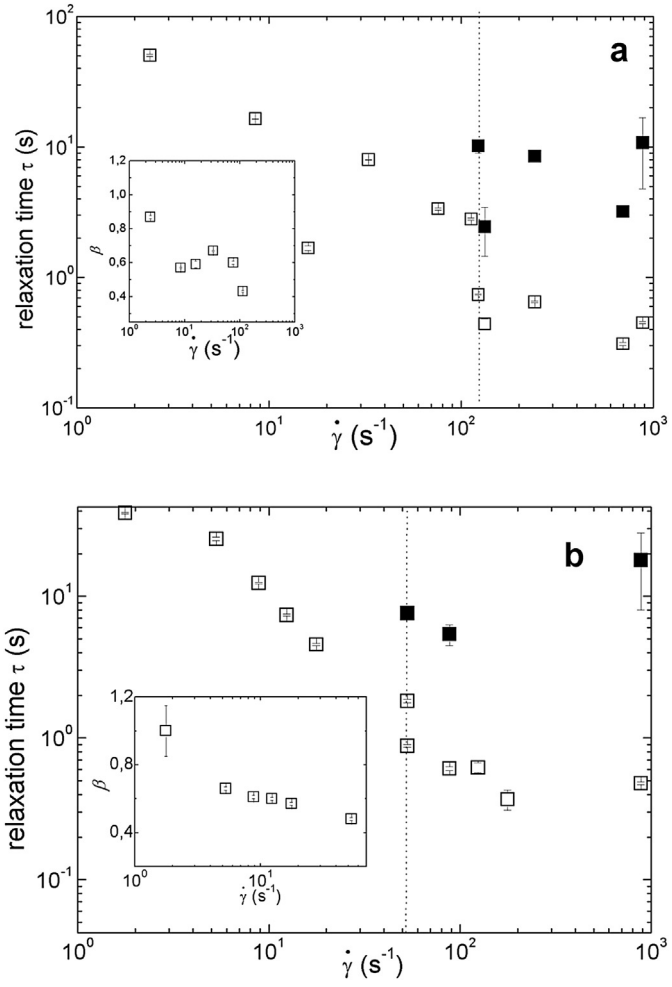

Fig. 9. Effect of shear rate on relaxation time of APC at: a) 90 °C and b) 120 °C. Vertical dashed lines indicate critical shear rate $\dot{\gamma}_c$. Insert: dependence of exponent β on shear rate.

At the lowest shear rate range, the stretched exponential function provides a good fit to the stress relaxation, with both characteristic relaxation time and exponent β decreasing with applied shear rate prior to flow cessation. The decline in β down to values as low as 0.4 suggests that the distribution of relaxation times becomes broader as the shear rate increases and that the relaxation process is progressively turning into a bimodal process. As such, above $\dot{\gamma}_c$ the faster relaxation time decreases with shear rate, whereas the longer relaxation time is virtually nondependent on shear history. In addition, the two relaxation times measured for shear rates larger than $\dot{\gamma}_c$ are essentially temperature independent, the faster being of the order of 0.5 s and the second one about 20 times slower.

Reminiscent of earlier reports on stress relaxation after flow at shear rates corresponding to the quasi-Newtonian plateau (regime II) [14], a strain scaling of the shear stress relaxation is observed for $\dot{\gamma} \leq \dot{\gamma}_c$. This is depicted in Fig. 10 for 120 °C and for representative stress relaxations plotted as a function of the strain $\dot{\gamma}t$ computed from the product of the applied shear rate and the time during relaxation. Also in harmony with earlier reports for comparable shear rates, no fast elastic relaxation is seen in Fig. 10 [14]. However, the strain scaling is lost after 200 strain units, in contrast with the scaling reported for full stress relaxation from shearing in regime II [14]. Note also that the strain scaling in stress relaxation is also lost for $\dot{\gamma} > \dot{\gamma}_c$ and that full stress relaxation takes more than 1000 strain units at larger shear rates. The scaling in stress relaxation has been assigned to the structural relaxation of the shear-induced texture

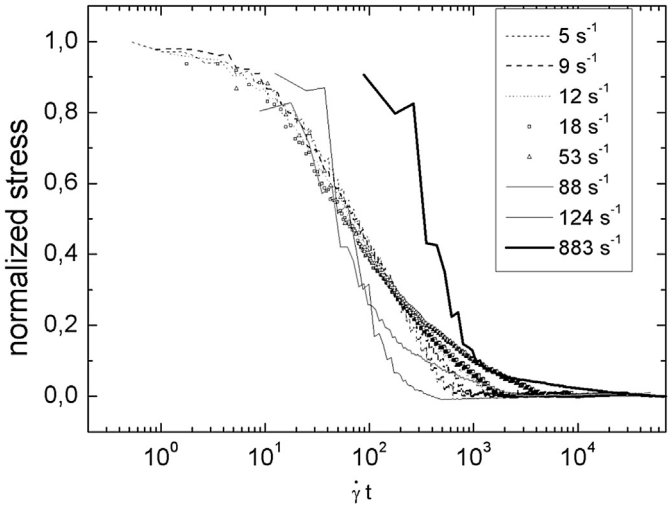

Fig. 10. Representative stress relaxation processes of APC, after flow at different shear rates, in normalized scale (measurements at 120 °C).

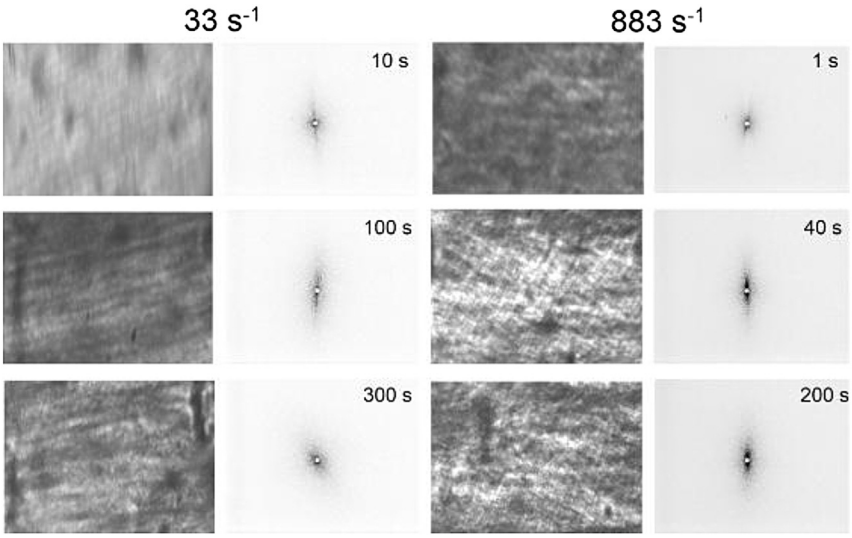

Fig. 11. Representative POM images and SALS patterns obtained at the times indicated, during relaxation of APC at 90 °C, upon cessation of steady shear rates of 33 s^{-1} (left) and 883 s^{-1} (right). Flow was applied along the vertical direction. The width of POM images corresponds to 470 micron.

(see for instance [14] and references therein). On the other hand, other reports showed that band texture formation after flow cessation in regime II was responsible for the stress relaxation in sheared APC [11,12]. To help addressing this unresolved issue and rationalizing the new set of rheological data displayed in Figs. 8–10 (obtained at larger shear rates than those reported so far), we shall now explore the structural relaxation of APC melt upon flow cessation.

In-situ POM and SALS analyses during stress relaxation offer a structural understanding of the stress relaxation of APC after application of large shear rates. Fig. 11 presents typical POM images and SALS patterns recorded at specific times during the relaxation of APC at 90 °C, after shear flow at 33 s^{-1} and 883 s^{-1}. Similar results were obtained at 120 °C. As seen in Fig. 12, a complex and rich band texture develops in the plane of the image, being defined by two directions – parallel and perpendicular – with respect to the shear flow direction (see schematics in Fig. 12).

The development of bands normal to the flow pictured in POM images is consistent with scattered intensity along the flow direction in SALS patterns. However, SALS only allows for a qualitative analysis, as no twin spots along the vertical axis could be pictured [11]. Thus, no spot spacing corresponding to band thicknesses could be computed. With time, the scattering pattern becomes more intense and thickens, suggesting the refining of the structure. Eventually, the SALS pattern disappears at longer times, while POM pictures still show bands (see Fig. 11 at 300 s). Overall, data in Fig. 11, together with the frozen band texture of the extrudates pictured in Fig. 5, show that the development of a complex band texture is responsible for the stress relaxation analyzed in Figs. 8–10. The results obtained from the quantitative analysis of POM images recorded during relaxation at 90 °C are presented in Figs. 13 and 14. Overall, similar results were obtained at 120 °C.

No picture analysis is available during the first second after flow cessation, hence no structural relaxation can be correlated with the faster shear stress relaxation time. The first conclusion from Fig. 13 is that bands formed perpendicular to the flow are significantly thicker than those developing in the flow direction. Second, bands thicknesses do not depend on shear history: bands of the order of 3 micron (perpendicular bands) and 1.5 micron (parallel bands) are pictured during relaxation following flow at shear rates smaller or larger than $\dot{\gamma}_c$. This result is in harmony with the band textures imaged in extrudates processed at different shear rates (see Fig. 5). Bands thicknesses pass through a maximum (which is less evident for parallel bands). The time at which the thickest bands are pictured does not depend on shear history: perpendicular bands are the thickest 50 s after flow cessation, whereas parallel bands are thickest after 70 s, for the two shear rates reported in Fig. 13. The time scale of this maximum matches the time needed to fully relax the stress: the longest characteristic time of the exponential stress relaxation is approximately 10 s for all shear rates (see Fig. 9). Thus, comparison of POM and rheological data suggests that stress relaxation upon flow cessation relates to the formation and width increase of parallel and perpendicular bands. At longer times, when no stress can be measured, bands still exist with thickness slightly decreasing with time. The harmony between stress and morphological relaxation also encompasses the absence of any shear history effect on the relaxation for the two shear rates considered here. The mechanism for band formation after shear cessation is still an unresolved issue [12,21]. However, results in Figs. 13 and 8 suggest that the time evolution of the band width shares similarities with the longest relaxation process in the shear stress: both are not related to the flow history. We can thus only conjecture that the nematic elasticity (Frank elasticity) of the APC melt is at the origin of the band width. Thus, this is an intrinsic APC property with no interplay with the shear history.

The time evolution of the bands orientation after flow cessation at 90 °C is displayed in Fig. 14. At longer times, the orientation angle of the parallel bands stabilizes at roughly 30–40° and for the perpendicular bands at 70–110°, for both temperatures (results not shown for 120 °C). The time evolution of the bands orientation follows the trend shown in Fig. 10: after the growth in band width, band orientation is locked. However, in contrast to the band width, a small effect of shear history is observed as larger angles are measured after flow at faster shear rates. These differences in orientation angle could explain the loss of strain scaling of the stress relaxation at longer time and for higher shear rates.

As mentioned above, the critical shear rate $\dot{\gamma}_c$ relates to a change in the extrudate swell and in the flow induced structure. Both are reminiscent of a change from tumbling to shear aligning behavior achieved only in the high shear rate regime and reported in numerous studies on lyotropic LCP [19,31]. These studies also reported a qualitative change in the stress relaxation occurring

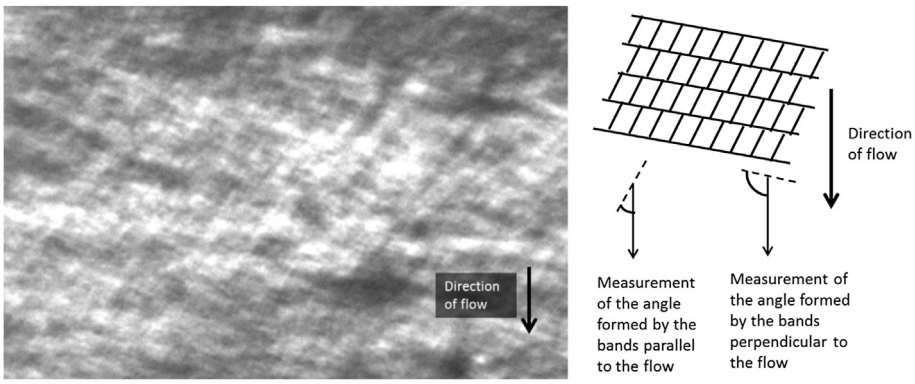

Fig. 12. Left: POM image of an APC band texture developed at 90 °C 40 s after flow cessation (shear rate 883 s^{-1}); right: schematic representation of the parallel and perpendicular bands with respect to the previous flow and definition of the corresponding band angles (right). The width of POM picture is 470 microns.

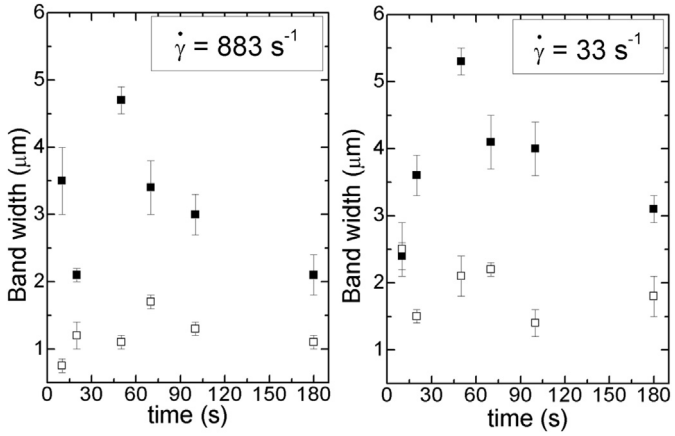

Fig. 13. Relaxation of bands width after flow cessation at 33 s^{-1} (right) and 883 s^{-1} (left): parallel bands (open symbols) and perpendicular bands (solid symbols) formed at 90 °C.

beyond the critical shear rate separating the tumbling and aligning regimes. However, since stress relaxation was monitored through small amplitude oscillatory shear [12], no quantitative analysis allowing extracting two relaxation times was provided. Thus, building on the fact that theories for liquid crystal polymers do not discriminate between lyotropic and thermotropic materials, and also building on the literature focusing on lyotropic LCP, we may identify the existence of two relaxation times in the stress with the transition from tumbling to aligning occurring at the critical shear rate $\dot{\gamma}_c$. Note that the strain scaling of the stress relaxation for shear rates below $\dot{\gamma}_c$ further supports this interpretation. The stress relaxation data in Fig. 9 suggest that the transition occurring at the critical shear rate is rather smooth as the relaxation process progressively evolves from a single relaxation to a broad relaxation process and eventually to two processes. Similarly, the APC melt is not fully aligned (see Fig. 4) even for shear rates where two relaxation times are found.

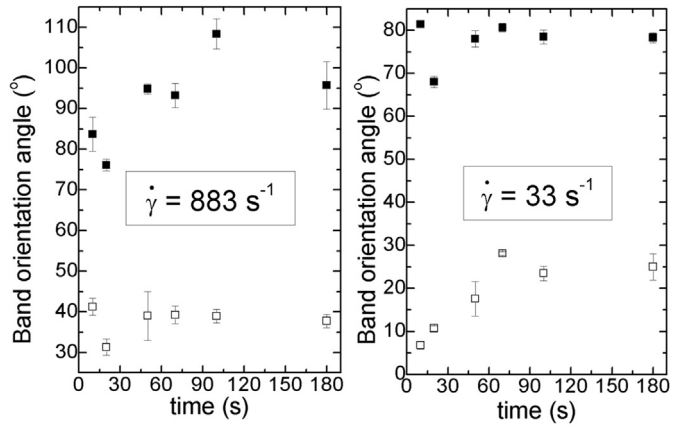

Fig. 14. Relaxation of bands orientation after flow cessation at 33 s^{-1} (right) and 883 s^{-1} (left): parallel bands (open symbols) and perpendicular bands (solid symbols) formed at 90 °C.

4. Conclusions

The rheological and structural characteristics of APC melt were studied over a wide range of shear rates. APC follows a shear thinning behavior with an exponent close to 0.6, for the whole shear rate range studied (up to 1000 s^{-1}). No full macromolecular alignment is ever achieved. Thus, no viscosity plateau arises in the flow curve. In-situ SALS patterns captured at larger shear rates showed two lobes oriented along the flow direction, whereas POM confirmed the shear-induced formation of a band texture in the direction perpendicular to the flow, in addition to bands aligned with the flow. Different structures are shear-induced at lower shear rates, as indicated by qualitatively different SALS patterns and POM images. The structural change is related with a change in the value of the negative extrudate-swell. This change occurs at a critical shear rate $\dot{\gamma}_c$ which is temperature dependent. The differences in the structures probed at different length scales within the slit suggest that 2 layers of APC nematic melt flow within the slit; these also explain the origin of the negative extrudate-swell.

A complex band texture develops during relaxation after flow cessation, showing bands oriented parallel and perpendicular to the flow direction. First, the bands widths grow with time and become thinner at longer times. The time evolution of bands thicknesses during relaxation does not depend on flow history, unlike the relaxation of bands orientation angles. The shear stress relaxation process shifts from one relaxation mode at smaller shear rates to two relaxation modes at larger shear rates. The transition between the two relaxation regimes occurs at the critical shear rate $\dot{\gamma}_c$, which was clearly identified by the transition in extrudate-swell behavior. These results suggest that both shear and normal stresses share the same relaxation process. The relaxation of the shear stress takes place on the time scale corresponding to the growth of the bands widths.

Acknowledgments

This work was partially supported by the Portuguese Science and Technology Foundation through projects, PTDC/CTM/099595/2008, PTDC/CTM/101776/2008, PTDC/CTM-POL/1484/2012 and UID/CTM/500025/2013. S.N. Fernandes and J.P. Canejo acknowledge FCT for grants SFRH/BPD/78430/2011 and SFRH/BPD/101041/2014, respectively. Funding for project "Matepro e Optimizing Materials and Processes", with reference NORTE-07-0124-FEDER-000037 FEDER COMPETE, is also acknowledged.

References

[1] G.V. Laivins, D.G. Gray, Liquid crystalline phase transition of a semiflexible polymer: acetoxypropyl cellulose, Macromolecules 18 (1985) 1753–1759.
[2] S.N. Bhadani, D.G. Gray, Cellulose-based liquid crystalline polymers: esters of (hydroxypropyl) cellulose, Mol. Cryst. Liq. Cryst. 99 (1983) 29–38.
[3] S.N. Bhadani, D.G. Gray, Liquid crystal formation from the benzoic acid ester of hydroxypropylcellulose, Die Makromolekulare Chemie, Rapid Commun. 3 (1982) 449–455.
[4] S. Onogi, T. Asada, Rheology and rheo-optics of polymer liquid crystals, Rheology (1980) 127–147. Springer.
[5] T. Asada, K. Toda, S. Onogi, Deformation and structural re-formation of lyotropic cholesteric liquid crystal of hydroxypropyl cellulose+ water system, Mol. Cryst. Liq. Cryst. 68 (1981) 1179–1194.
[6] M. Mitov, N. Dessaud, Going beyond the reflectance limit of cholesteric liquid crystals, Nat. Mater. 5 (2006) 361–364.
[7] Y. Geng, P.L. Almeida, S.N. Fernandes, C. Cheng, P. Palffy-Muhoray, M.H. Godinho, A cellulose liquid crystal motor: a steam engine of the second kind, Sci. Rep. 3 (2013).
[8] P.L. Almeida, M. Godinho, M. Cidade, J. Figueirinhas, Electro-optical properties of cellulose based PDLC type cells: dependence on the type of diisocyanate cross-linking agent used, Mol. Cryst. Liq. Cryst. 368 (2001) 121–128.
[9] M. Godinho, J. Canejo, G. Feio, E. Terentjev, Self-winding of helices in plant tendrils and cellulose liquid crystal fibers, Soft Matter 6 (2010) 5965–5970.
[10] M. Cidade, C. Leal, M. Godinho, A. Martins, P. Navard, Rheological properties of acetoxypropylcellulose in the thermotropic chiral nematic phase, Mol. Cryst. Liq. Cryst. 261 (1995) 617–625.
[11] J.-B. Riti, M. Cidade, M. Godinho, A. Martins, P. Navard, Shear induced textures of thermotropic acetoxypropylcellulose, J. Rheol. 41 (1997) 1247–1260.
[12] P. Harrison, P. Navard, M.T. Cidade, Investigation of the band texture occurring in acetoxypropylcellulose thermotropic liquid crystalline polymer using rheo-optical, rheological and light scattering techniques, Rheol. Acta 38 (1999) 594–605.
[13] A.F. Martins, Theory of shear rate dependence of viscosity and normal stress differences in nematic LC polymers, in: C. Carfagna (Ed.), Liquid Crystalline Polymers, Pergamon Press, UK, 1994, pp. 153–162.
[14] F. Beekmans, A. Gotsis, B. Norder, Transient and steady-state rheological behavior of the thermotropic liquid crystalline polymer Vectra B950, J. Rheol. (1978-present) 40 (1996) 947–966.
[15] H. Langelaan, A. Gotsis, A.P. De Boer, On the linearity of the pressure drop during flow of thermotropic LCPs in slits and capillaries, J. Rheol. (1978-present) 38 (1994) 1353–1368.
[16] K.F. Wissbrun, Note: negative extrudate swell of liquid crystal polymers, J. Rheol. 38 (1994) 247–252.
[17] A. Romo-Uribe, Molecular orientation in sheared molten thermotropic random copolyester, Rheol. Acta 46 (2007) 1139–1152.
[18] S. Rendon, W.R. Burghardt, R.A. Bubeck, Orientation dynamics in commercial thermotropic liquid crystalline polymers in transient shear flows, Rheol. Acta 46 (2007) 945–956.
[19] R. Larson, The Structure and Rheology of Complex Fluids, Oxford University Press, New York, 1999, p. 546.
[20] A. Donald, C. Viney, A. Windle, Banded structures in oriented thermotropic polymers, Polymer 24 (1983) 155–159.
[21] S.J. Picken, D.J. Sikkema, H. Boerstoel, T.J. Dingemans, S. van der Zwaag, Liquid crystal main-chain polymers for high-performance fibre applications, Liq. Cryst. 38 (2011) 1591–1605.
[22] P.F. Teixeira, L. Hilliou, J.A. Covas, J.M. Maia, Assessing the practical utility of the hole-pressure method for the in-line rheological characterization of polymer melts, Rheol. Acta 52 (2013) 661–672.
[23] P.F. Teixeira, J.M. Maia, J.A. Covas, L. Hilliou, In-line particle size assessment of polymer suspensions during processing, Polym. Test. 37 (2014) 68–77.
[24] S.G. Hatzikiriakos, J.M. Dealy, Start-up pressure transients in a capillary rheometer, Polym. Eng. Sci. 34 (1994) 493–499.
[25] J.M. Dealy, On the significance of pressure relaxations in capillary or slit flow, Rheol. Acta 34 (1995) 115–116.
[26] R.H. Colby, D.C. Boris, W.E. Krause, S. Dou, Shear thinning of unentangled flexible polymer liquids, Rheol. Acta 46 (2007) 569–575.
[27] J.D. Ferry, Viscoelastic Properties of Polymers, Wiley, New York, 1980, p. 258.
[28] T. Kume, T. Hashimoto, T. Takahashi, G.G. Fuller, Rheo-optical studies of shear-induced structures in semidilute polystyrene solutions, Macromolecules 30 (1997) 7232–7236.
[29] R.D. Gilbert, R.A. Venditti, C. Zhang, K.W. Koelling, Melt spinning of thermotropic cellulose derivatives, J. Appl. Polym. Sci. 77 (2000) 418–423.
[30] J.E. Taylor, A. Romo-Uribe, M.R. Libera, Molecular orientation gradients in thermotropic liquid crystalline fiber, Polym. Advan. Technol. 14 (2003) 595–600.
[31] R. Larson, The Structure and Rheology of Complex Fluids, Oxford University Press, New York, 1999, p. 461.
[32] C. Sena, M. Godinho, C. Oliveira, A.F. Neto, Liquid crystalline cellulosic elastomers: free standing anisotropic films under stretching, Cellulose 18 (2011) 1151–1163.